Ratiometric Raman and Luminescent Thermometers Constructed from Dysprosium Thiocyanidometallate Molecular Magnets

*Kunal Kumar, Olaf Stefanczyk, Szymon Chorazy, Koji Nakabayashi, and Shin-ichi Ohkoshi**

Molecular crystals acting as temperature sensors, designed for multiple measurement techniques, can be a promising pathway for self-calibrating thermometers. The molecular assemblies $[Dy_x^{III}Y_{1-x}^{III}(phen)_2(\mu\text{-}OH)_2(H_2O)_2]\cdot[Au^I(SCN)_2]_2\cdot phen\cdot 0.5MeCN\cdot 0.5H_2O$ (x = 0, 0.1, 0.02; phen = 1,10-phenanthroline) which contain weakly bonded lanthanide(III) and Au(I) metal complexes are reported. They have Raman scattering in the low-frequency (LF) region with sharp peaks, one of the prerequisites to design Raman thermometers. The Raman thermometric behaviors are characterized by three vibrational bands, and their thermal sensitivity is compared with their emission thermometric ability. The LF phonon linked with the Au⋯Au vibration helps increase the thermometric sensitivity of emission and Raman thermometers. Additionally, magnetically diluted complexes containing both Dy^{3+} and Y^{3+} ions are prepared to demonstrate the effect of temperature sensing capability through Raman and emission spectroscopy among isostructural mixed-metal materials. Compounds are immersed inside various benchtop solvents to unravel the robustness and functioning of Raman thermometers. Furthermore, they reveal single-molecule magnet properties, which disclose the effect of LF phonons on the spin relaxation process. Therefore, the reported molecular materials are Raman and luminescent thermometers, and they contain a molecular magnetic center with thiocyanidoaurate ions playing a critical role due to their emissive and Raman activities.

K. Kumar, O. Stefanczyk, S. Chorazy, K. Nakabayashi, S.-i. Ohkoshi
Department of Chemistry, School of Science
The University of Tokyo
7-3-1 Hongo, Bunkyo-ku, Tokyo 113-0033, Japan
E-mail: ohkoshi@chem.s.u-tokyo.ac.jp
S. Chorazy
Faculty of Chemistry
Jagiellonian University
Gronostajowa 2, Krakow 30-387, Poland

The ORCID identification number(s) for the author(s) of this article can be found under https://doi.org/10.1002/adom.202201675.

1. Introduction

Molecular materials like metal–organic frameworks, supramolecular assemblies, and Prussian blue analogs have been extensively studied for various physical properties.[1] High-performing magnetic, luminescent, conductive, and non-linear optical materials have been reported from the above class of metal complexes.[2] The bottom-up approach employed in obtaining these molecular materials provides impeccable control with a judicious selection of precursors to combine two or more properties within one system.[3,4] Among them, luminescent complexes showing diverse emission colors and white luminescence have been investigated.[5] Additionally, the temperature dependence of emission peaks intensities and/or area has been employed in advanced contactless optical thermometry,[6] the achievements of which to date are the culmination of eight decades of rigorous research work.[7] They possess high sensitivity, up to several % K^{-1} in a certain temperature range of working temperature range, and nano-/microspatial resolution using super-resolution fluorescence microscopy.[8] Another method of optical thermometry that is relatively novel and less explored, especially among molecular compounds, is non-contact Raman thermometry.[9] It can be performed on several micrometer-sized crystals, thin films, multi-layered samples, nanoparticles, and powder samples, providing specific relations between the structure and properties of the material at a given temperature.[9d,10] Moreover, it can also be applied in conditions in which fluorescence thermometry could not be realized due to experimental limitations, such as solvent ultraviolet (UV) cutoff for excitation light (e.g., 330 nm for acetone), interference between a sample and phosphors, and photodamaging and heating by UV excitation light. In this context, Raman thermometry enables the testing of various materials in liquid environments as well as in organic solvents; in particular, metal complexes sensitive to loss of crystallization or absorbed solvent; compounds reacting with air or moisture protected by

**ADVANCED
SCIENCE NEWS**
www.advancedsciencenews.com

**ADVANCED
OPTICAL
MATERIALS**
www.advopticalmat.de

immersing in oil; materials sensitive to high energy UV radiation (e.g., photochromic materials); and for in vitro tests of biological samples in a solvent medium, important for the course of cryopreservation and the detection of temperature limit tests for biological systems (e.g., studies of extremophile organisms in their natural environment conditions). Recent discoveries have shown that Raman thermometry can be a useful tool to monitor the cellular temperature during photothermal therapy of tumors.[11] A similar application has also been realized for luminescent thermometers in the field of nanomedicine.[12] However, the application of emissive thermometers to the non-luminescent probe is impossible. On the contrary, vibrational features are more ubiquitous in the materials that feature in the research of Balaji Srinivasan et al.[13a] They have shown that the temperature of overhead power transmission cables can be monitored in real-time mode through Raman thermometry.[13] It is worth mentioning that the first attempts to develop synergistic Raman and photoluminescence thermometers have been conducted, but these studies were limited only to the detection of Raman active bands through emission spectroscopy, not direct Raman spectroscopy.[14]

Raman thermometry works based on the vibrational peak shifts with temperature or by taking the ratio of the Raman band at the anti-Stokes (aS) and Stokes (S) positions. The second working principle exploring the aS/S ratio distinguishes Raman thermometry from infrared thermometry in terms of increased sensitivity.[9a,15] The efficiency of the anti-Stokes process is directly proportional to the population of excited vibrational modes which follows the Boltzmann distribution with temperature. A good Raman thermometer should possess a large Raman scattering cross-section, high Raman scattering in the low-frequency (LF) region, sharp peaks, and low absorbance of material concerning the exciting source.

Keeping the above materials research trend in mind, taking also into account the magnetic material perspective, we selected trivalent lanthanide ions (Ln(III)) as one of the precursors to include the emission and magnetic properties simultaneously.[2b,16] Ln(III) complexes have diverse luminescence colors and exhibit single-molecule magnet (SMM) properties.[16] Ln(III)-containing complexes reveal SMM behavior due to their strong magnetic anisotropy generating the energy barrier (ΔE) of spin relaxation. For such opto-magnetic lanthanide complexes, studying the vibrational signature in the LF region for Raman active modes through LF Raman spectroscopy can enhance our understanding of the dependence of physical properties (magnetic, optical) on structural changes.[17] Raman spectroscopy in the LF region has been used to detect various bonds of Au atoms in gold clusters, vibrational modes of pharmaceutical crystals, and phonons of graphene.[18]

In this regard, Raman spectroscopy applied to a temperature sensor in the LF region (especially below 1 THz) has not been reported. Besides, a ratiometric thermometer (both Raman-type and emission-type) can be a great choice as a self-calibrating thermometer that uses the spectral intensity ratio for contactless thermal sensing. It is vital as many Raman thermometers explore the band shift rather than the ratio between the intensities of specific Raman peaks. Further utilization of two different spectroscopy techniques (Raman and luminescent) can provide more reliable information about the local temperature

of the system by reducing measurement errors and measurement repeatability. Motivated to explore the Raman scattering for opto-magnetic molecular complexes, we prepared Dy(III)-containing molecular materials with the formula of $[Dy_x^{III}Y_{1-x}^{III}(phen)_2(\mu\text{-}OH)_2(H_2O)_2]\cdot[Au^I(SCN)_2]_2\cdot phen\cdot 0.5MeCN\cdot 0.5H_2O$ [$x = 0$ (DyAu), $x = 0.1$ (Dy$_{0.1}$Y$_{0.9}$Au), $x = 0.02$ (Dy$_{0.02}$Y$_{0.98}$Au)], where phen is 1,10-phenanthroline. We selected this system as it has sharp Raman scattering peaks in the LF region revealed for the Y(III)- and Gd(III)-containing analogous compounds, one of the prerequisites for a good Raman thermometer.[5e] Further, emission properties at variable temperatures were investigated and, thanks to the presence of emissive Dy^{3+} ions, luminescent thermometric properties were observed. Therefore, we compared the thermometric sensitivity of the emission and Raman spectroscopic features for all the complexes. Additionally, we demonstrated Raman thermometer behavior's applicability under various solvent conditions, in which classical fluorescent thermometers rarely operate,[6a-c] by measuring the Raman spectra for submerged solid crystals. Finally, due to the presence of paramagnetic Dy^{3+} ions, we observed the SMM behavior for all compounds, which improved with magnetic dilution and has been correlated with the vibrational characteristics detectable in Raman spectroscopy.

2. Result and Discussion

2.1. X-Ray Crystallography

Colorless crystals of DyAu, Dy$_{0.1}$Y$_{0.9}$Au, and Dy$_{0.02}$Y$_{0.98}$Au were obtained from the mother solution containing an acetonitrile/water mixture (see Experimental Section, Supporting Information). Single-crystal X-ray diffraction (SC-XRD) measurements for DyAu revealed that the material is centrosymmetric, crystallizing in the triclinic P–1 space group (**Figure 1**, Figures S1 and S2, and Tables S1 and S2, Supporting Information). Trimetallic mixed assemblies were prepared by mixing the appropriate amount of Ln(III) precursors and confirmed its perfect isostructural with DyAu by powder X-ray diffraction measurement (Figure S3, Supporting Information). Each Dy(III) center coordinates two water molecules, two hydroxide ions, and two phen molecules. These gave four oxygen and four nitrogen atoms in the first coordination sphere to form a triangular dodecahedron geometry, confirmed by the Continuous Shape Measure (CShM) analyses (Tables S3, Supporting Information). The two cationic components $\{Dy^{III}(phen)_2(H_2O)_2(\mu\text{-}OH)_2\}^{2+}$ are connected through hydroxide molecular bridges to yield a dimeric unit with Dy(III) separation of 3.73 Å. The anionic $\{[Au^I(SCN)_2]^-\}_2$-moiety consists of two Au(I) atoms, with two S-coordinated thiocyanide ions each. The Au–Au distance between two bis(thiocyanido)gold(I) units is 3.19 Å at 90 K, which is longer than the observed distance in Y(III)- and Gd(III)-based analogous matrices.[5e] This implies that as the atomic radius of lanthanide ions is shrinking within the lanthanide series, the Au–Au distance is expanding as a result, and thus the aurophillic interaction is gradually weakened. Notably, crystallographic studies revealed a significant increase in the Au–Au distance from 3.19 Å at 90 K to 3.31 Å at 300 K (Tables S2, Supporting Information), indicating that thermometric
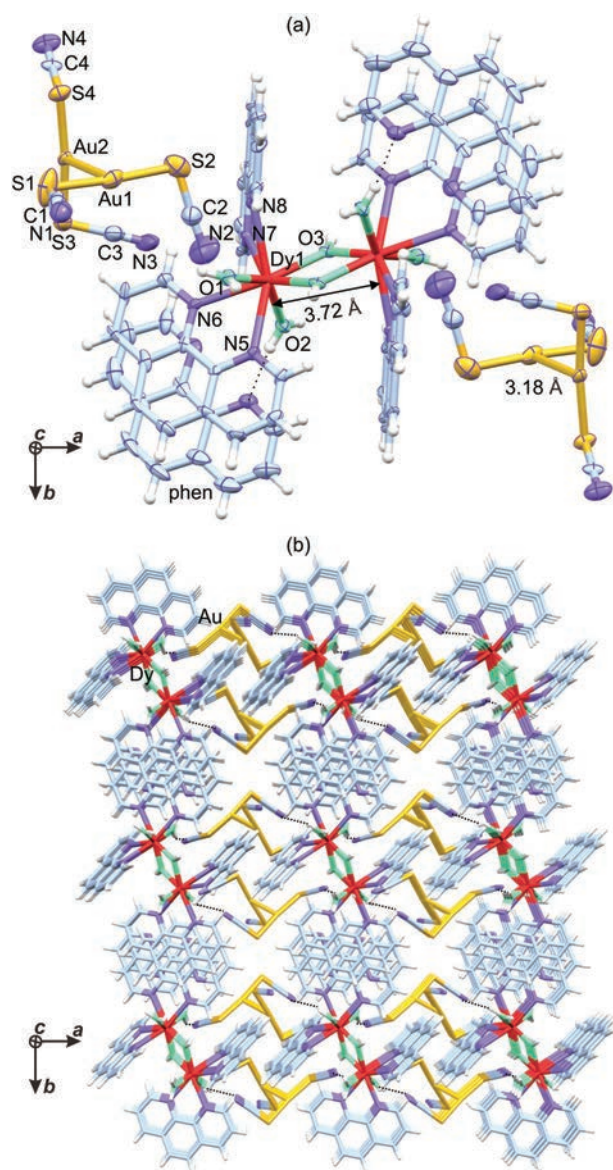
Figure 1. Crystal structure of DyAu: a) the view of two lanthanide complexes bridged by hydroxide ligands, crystallizing together with thiocyanidoaurate dimeric units, and non-coordinated phen molecules, b) the view of the crystal packing along the crystallographic c axis.

properties are associated with structural changes. Nevertheless, weak diffraction of crystals prevents determining the full temperature dependence.

The molecules of crystallization in DyAu include phen, water, and acetonitrile. They help in stabilizing the supramolecular assemblies through various hydrogen bonds involving hydrogens of water and nitrogens of thiocyanide ions, and between water and non-coordinated phen molecule. Along the crystallographic c axis, one of the coordinated phen, and crystallization phen molecules form π–π stacking, with the closest distance between their centroids of 3.62 Å. The composition and isostructurality of the whole series of materials, DyAu, $Dy_{0.1}Y_{0.9}Au$, and $Dy_{0.02}Y_{0.98}Au$, are confirmed through thermogravimetric analyses, indicating the amount of coordinated and

crystallization solvent molecules calculated from the CHNS elemental analyses (Figure S4, Supporting Information). Infrared and Raman spectroscopy were performed for all compounds, showing the presence of the cyanido stretching vibrations as well as the broad O–H vibrational bands (Figures S5–S6, Supporting Information).
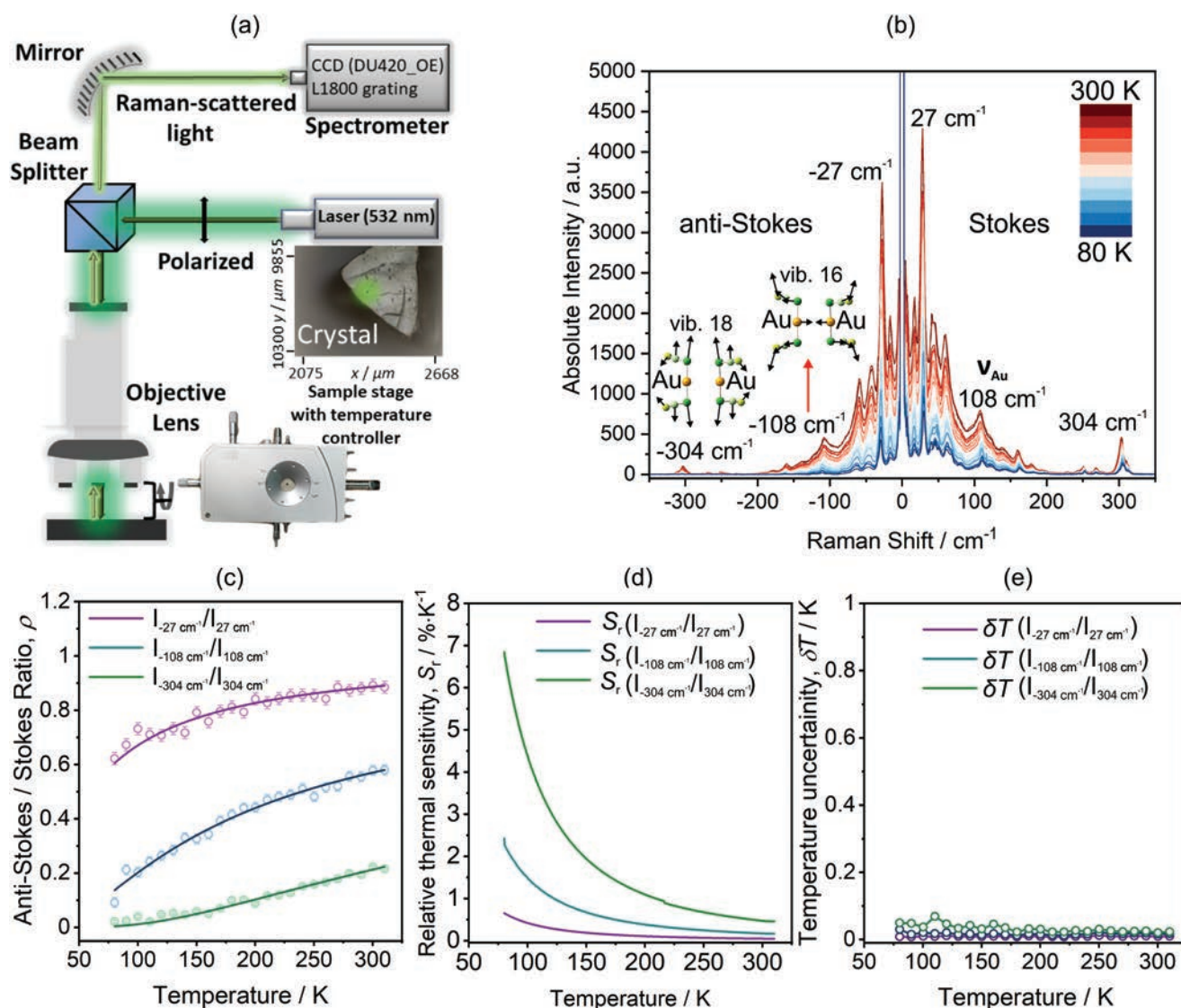
2.2. Raman Thermometry

Further, to understand the vibrational features in the LF region for all the compounds, we performed Raman spectroscopy for the single crystals of DyAu, $Dy_{0.1}Y_{0.9}Au$, and $Dy_{0.02}Y_{0.98}Au$ (**Figure 2** and Figures S7–S11, Supporting Information). The 532 nm laser light was used to probe the Raman active modes by observing the Stokes and anti-Stokes Raman shifts (Figure 2). The spectra have several peaks assigned to the vibrations of bis(thiocyanido)gold(I) moieties and the phen molecule, present in the crystal structure (Figures S7 and S8, Table S4, Supporting Information). The peak centered around 108 cm^{-1} correlates with the vibrational modes of Au···Au stretching vibration, which shrinks upon cooling, as confirmed by the shift of this peak in the high-frequency region. The peak intensity of these phonons with temperature decreases at different rates depending upon the energy of vibrations. The peak intensity of high-energy Raman shift (>500 cm^{-1}) saturates at higher temperatures (close to room temperature). However, the peak intensity of low-energy stretching frequency decreases following the Boltzmann distribution.[5e] This makes vibrational peaks in the LF region ideal for thermometric characterization in the wide temperature range. Therefore, we selected three vibrational peaks centered at 27, 108, and 304 cm^{-1} to represent the energy spectrum of vibration from below 33 cm^{-1} (below 1 THz) through around 99 cm^{-1} (3 THz) up to ≈303 cm^{-1} (9 THz) to investigate its thermometric behavior.

To precisely determine the temperature, the ratio of scattered anti-Stokes and Stokes Raman signal (also referred to as ρ) corresponding to the abovementioned vibrational frequency is calculated and fitted with the Equation (1).[9a,10a]

$$\frac{I_{aS}}{I_S} = C\left(\frac{v_L}{v_P}\right)^3 e^{\left(\frac{-hv_P}{k_B T}\right)} \tag{1}$$

where I_{aS} and I_S are the peak intensity of anti-Stokes and Stokes Raman shifts, respectively, C is the calibration constant, v_L (s^{-1}) is the frequency of the laser, v_P (s^{-1}) frequency of the vibrational band, h (J s^{-1}) is Planck's constant, k_B (J K^{-1}) is the Boltzmann's constant, and T (K) is the temperature. Equation (1) suggests that ρ depends on the frequency of the incident laser as well as on the use of the detection method. The ρ is proportional to the quadruple of the ratio of incident laser frequency and frequency of vibrational mode when energy-based detection systems are used.[10a] However, the charge-coupled device based detector proportionality relation takes the expression of Equation (1). The fitted results are presented in Figure 2 and Table S5 (Supporting Information) for the DyAu complex. The obtained calibration constant (C) for DyAu lies in the range of 1.01–0.83, and the smaller value is related to high energy vibrational shift, which stays contrary to the diluted sample $Dy_{0.02}Y_{0.98}Au$. The

ADVANCED
SCIENCE NEWS
www.advancedsciencenews.com

ADVANCED
OPTICAL
MATERIALS
www.advopticalmat.de

Figure 2. a) The scheme depicts the Raman spectra measurement method, using the cryogenic stage. b) Temperature-dependent Raman scattering for DyAu in the temperature range of 300–80 K. c) Experimental anti-Stokes/Stokes ratios in the range of 300–80 K for the Raman vibrational modes at 27 cm^{-1} (top), 108 cm^{-1} (middle), and 304 cm^{-1} (bottom) were collected after being excited by a 532 nm laser source. d) The calculated thermal sensitivity and e) temperature uncertainty for the temperature range of 300–80 K. The dotted plots in (c) represent experimental results and are fitted with Equation (1), thermal sensitivity in (d) is calculated with Equation (2), and the dotted-dashed line in (e) is calculated with Equation (3). The inset of (b) depicts the vibrational modes associated with bis(thiocyanido)gold(I) moieties for peaks centered around 108 and 304 cm^{-1} calculated based on density functional theory. Details about the Raman active vibrational modes are given in Table S4 (Supporting Information).

large C for 304 cm^{-1} (1.03) vibrational peak in the compound with a high concentration of Y(III) can be correlated with the smaller Au···Au bond distance (3.105 Å).[5e] The calculated C values for the 108 cm^{-1} phonon modes are closer to reported values for the 143 cm^{-1} vibrational peak in TiO$_2$.[12a] Interestingly, the determined ρ value is the largest for the 27 cm^{-1} vibrational band for all temperature ranges, followed by the 108 cm^{-1}. This observation implies that the population of scattered light with high energy photons (resulting in the anti-Stokes Raman shift) after coupling LF molecular vibrations with incident light is larger than for the higher energy stretching vibrations within the same system. The experimental ρ value lies in the range of 0.89–0.62, 0.58–0.10, and 0.22–0.02 for the vibrational band

at 27, 108, and 304 cm^{-1}, respectively, for all compounds. The ratio (ρ) starts to saturate as the temperature of the surroundings approaches 80 K for the 304 cm^{-1}. We evaluated the relative thermal sensitivity (S_r) using Equation (2) by utilizing the fitted curve from the ρ versus T dependence to further examine the thermometric accuracy:

$$S_r = \frac{\left(\frac{\partial \rho}{\partial T}\right)}{\rho} \times 100 \tag{2}$$

The evaluated sensitivity is listed in Table S6 (Supporting Information). Thermometric sensitivity increases for all

**ADVANCED
SCIENCE NEWS**
www.advancedsciencenews.com

**ADVANCED
OPTICAL
MATERIALS**
www.advopticalmat.de

stretching frequencies as temperature decreases from 300 to 80 K, reaching maxima at the lowest temperature. Maximum sensitivity (6.84% K^{-1}) is observed for the 304 cm^{-1}, followed by 108 cm^{-1} (2.42% K^{-1}), and lowest for the 27 cm^{-1} (0.65% K^{-1}) at 80 K. The opposite trend for the sensitivity compared with temperature-dependent of ρ can be explained by the fact that the rate of depopulation of the vibrationally excited state is faster for the 304 cm^{-1} stretching frequency when compared with the lower energy vibrational bands. The observed sensitivity is higher than the recently reported Raman thermometer (based on TiO_2) in the temperature range of 280–325 K, which lies in the range of 0.26–0.1% K^{-1}.[10a] We also calculated the temperature uncertainties using Equation (3), which suggests that they lie below 1 K for the broad temperature region (Figure S9, Supporting Information):

$$\delta T = \frac{\left(\frac{\delta\rho}{\rho}\right)}{S_r} \qquad (3)$$

where $\frac{\delta\rho}{\rho}$ is a relative error in the determination of ρ calculated after considering the spectral resolution and its background noise. Similar values of thermometric parameters were found among all assemblies thanks to their isostructurality, while the tuning of these parameters can be realized by the selection of vibrational peak frequency (Table S6, Supporting Information).

Additionally, to understand the repeatability of these parameters, we performed similar experiments on the crystals of $Dy_{0.1}Y_{0.9}Au$ and $Dy_{0.02}Y_{0.98}Au$ under the same measurement conditions (Figures S10 and S11, Supporting Information). Both complexes have ρ lying in a similar range for all three vibrational modes as well as their relative thermal sensitivity (Table S6, Supporting Information). This implies that the isostructural compounds' vibrational signature in the LF region that uniquely identifies their crystal lattice packing follows a similar trend of thermal cooling. For the first time, we present a systematic study of molecular assemblies with similar crystal packing exhibiting an analogous thermal-dependent Raman scattering process.

2.3. Raman Thermometry in Solvents

The observation of a temperature-dependent Raman signal related to the various vibrational modes of the single crystalline sample motivated us to look for its potential application. Various forms of application can be envisioned, such as detecting the first-order phase transitions for other compounds in a wide temperature range (e.g., liquid–solid boundary of azeotropic mixtures) by mixing a Raman thermometer with the material having an unknown transition temperature. Another form of application can be to test the workability of these Raman thermometers in the presence of various gases, liquid solvents, solid mixtures, etc. Therefore, to demonstrate the introductory applications scheme, we tested the Raman thermometric effect for the crystals immersed in a few benchtop solvents like water, methanol, ethanol, isopropanol, acetone, hexane, and
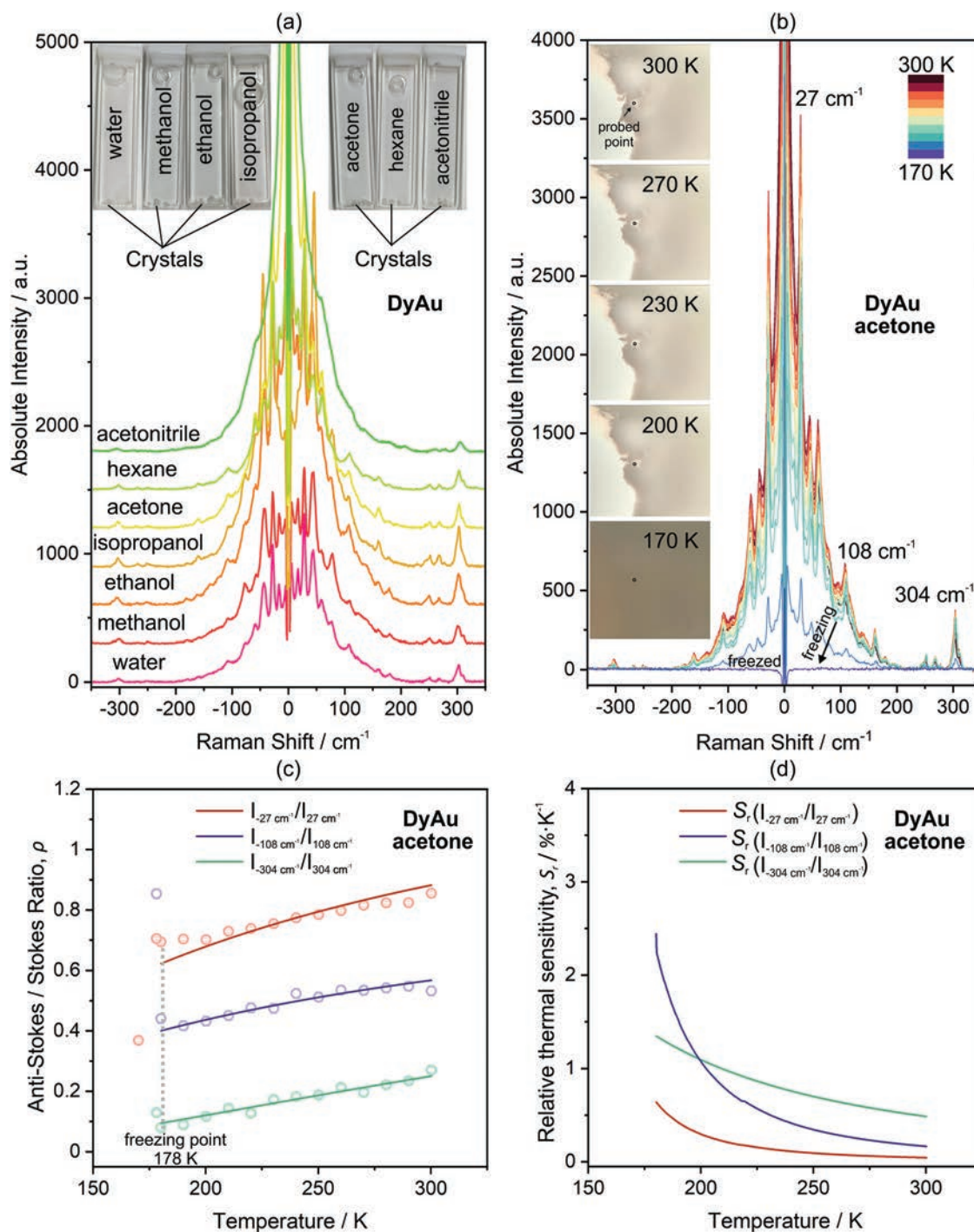
acetonitrile. The colorless crystals of DyAu were placed inside a thin cuvette, followed by the addition of ≈4 mL of solvent to fill up the container, as depicted in **Figure 3**. This study, for the first time, shows the interference of solvents on the LF Raman signal of known materials in the presence of various solvents while detecting the phase transition of liquids around their freezing point. The phase changes are also confirmed by the picture of frozen solvents near their known freezing temperatures (Figure 3, Figures S12–S18, and Table S7, Supporting Information). The Raman spectrum measured after the freezing point suggests that solidified solvent inhibits crystal excitation under the same optical path, leading to the disappearance of scattering from DyAu.

The detected Raman signal in the LF region for the different solvents demonstrates the same sharp peak with a similar background as the pristine material except for the measurement in acetonitrile. The DyAu in acetonitrile exhibits visible peaks related to the known vibrations. However, it has a very large background below 50 cm^{-1} (Figure S17, Supporting Information). Therefore, we performed full thermometric characterization of DyAu in all other solvents by evaluating the anti-Stokes to Stokes ratio as a function of temperature. The Raman signal decreases with temperature in all solvents. The ratio ρ is fitted with Equation (1), indicating the non-intervention of the solvents. The maximum thermal sensitivity corresponding to all the stretching vibrations is observed close to the freezing temperature, and the minimum sensitivity is observed at 300 K, comparable with the original material. Maximum sensitivity observed is 2.44% K^{-1} at 273, 176, 170, 180, 180, and 180 K for the DyAu in the water, methanol, ethanol, isopropanol, acetone, and hexane, respectively, for the 108 cm^{-1} vibrational band related to the Au···Au motion (Table S8, Supporting Information). In conclusion, DyAu is a thermometer that works under different solvent conditions to sense the surrounding temperature before freezing the corresponding solvent.

2.4. Emission Thermometry and Its Comparison with Raman Thermometry

The solid-state UV–vis–NIR absorption spectra indicate strong absorption in the UV region limited to the 400 nm ascribable to Au(I) centers (Figure S19, Supporting Information). In the visible and NIR region, very weak sharp peaks are observed for the DyAu related to the direct excitation of Dy(III) ion, which diminishes upon dilution with Y(III) ions for $Dy_{0.1}Y_{0.9}Au$ and $Dy_{0.02}Y_{0.98}Au$. The absence of absorption near 532 nm also helped preserve the crystalline sample under intense laser irradiation for Raman spectrum collection.

Apart from vibrational thermometry, these assemblies exhibit visible emission originating from Dy(III) ions and excimer Au(I) entities, observed over a broad temperature region of 10–300 K (Figure 4). The excitation by 325 nm light yielded two sets of peaks in all three complexes (Figure 4a–c). The first set of broad peaks centered around 460 and 510 nm originates from the excimers of $\{[Au(SCN)_2]^-\}_2$, and the second set of sharp peaks located at 480, 575, and 660 nm comes from the f–f electronic transitions of Dy^{III} centers, $^4F_{9/2} \rightarrow {}^6H_{15/2}$, $^6H_{13/2}$, and $^6H_{11/2}$ transitions, respectively.[5e] The excitation spectrum

**ADVANCED
SCIENCE NEWS**

www.advancedsciencenews.com

**ADVANCED
OPTICAL
MATERIALS**

www.advopticalmat.de

Figure 3. a) Raman scattering for DyAu submerged in various solvents as specified at 27 °C, and b) the temperature-dependent Raman shift for DyAu immersed in acetone for the temperature range of 300–170 K. c) Experimental anti-Stokes/Stokes ratios in the range of 300–170 K for the Raman vibrational modes at 27 cm^{-1} (top), 108 cm^{-1} (middle), and 304 cm^{-1} (bottom) were collected after being excited by a 532 nm laser source. d) The calculated thermal sensitivity for the temperature range of 300–170 K. The dotted plots in (c) are fitted with Equation (1), and the thermal sensitivity in (d) is calculated with Equation (2). The inset of (a) contains the picture of the cuvette with the indicated solvents utilized to drown the crystals of DyAu visible at the bottom of the container. The inset of (b) shows the picture of a single-crystal taken just before the measurement by the microscopic camera attached to the equipment at the indicated temperature. Black circles reveal the point of measurement. The dotted vertical line in (c) points to the freezing temperature of acetone.

corresponding to different emissive peaks, within the whole series of materials, consists of a similar broad peak centered around 365 nm with variable broadening. The excitation is assigned mainly to the singlet-to-singlet ($S_0 \rightarrow S_1$) and singlet-to-triplet ($S_0 \rightarrow T_1$) transitions within dimers of bis(thiocyanido) gold(I) entities (Figures S20–S22, Supporting Information).
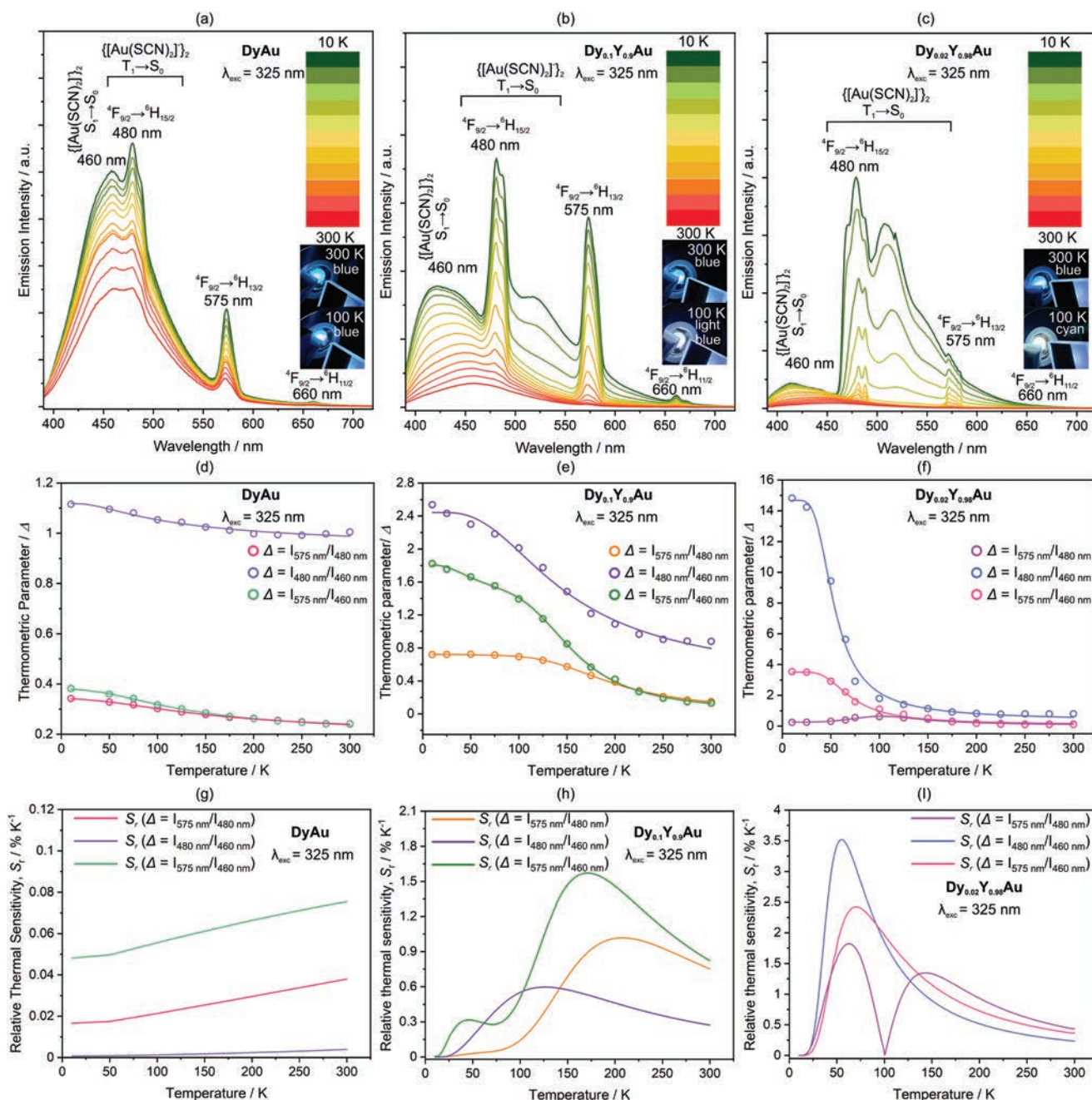
Figure 4. Solid-state emission spectra and the observed emission color at the indicated temperatures for a) DyAu, b) $Dy_{0.1}Y_{0.9}Au$, and c) $Dy_{0.02}Y_{0.98}Au$ measured in the temperature range of 10–300 K for the excitation wavelengths of 325 nm. The thermometric parameter (Δ) for the indicated emissive peak ratios in the temperature range of 10–300 K of the compounds d) DyAu, e) $Dy_{0.1}Y_{0.9}Au$, and f) $Dy_{0.02}Y_{0.98}Au$ for irradiation light of 325 nm. The calculated thermal sensitivity for the corresponding fitted curves of Δ for g) DyAu, h) $Dy_{0.1}Y_{0.9}Au$, and i) $Dy_{0.02}Y_{0.98}Au$. The fitted lines in (d)–(f) follow Equation (4).

Interestingly, the emission pattern for all of the assemblies is different in the context of the strength of emission originating from the Au(I) excimers (Figure 4a–c). The temperature-dependent spectrum of DyAu indicates that the energy absorbed by Au(I) centers is partially transferred to neighboring Dy(III) ions. At low temperatures, the Dy(III) emission peaks become sharper and stronger due to the deactivation of non-radiative thermal relaxation pathways. This is also supported

by the lack of emission peak originating from triplet-to-singlet electronic states of $\{[Au(SCN)_2]^-\}_2$, which was visible in the analogous Y(III) or Gd(III) matrices.[5e] Therefore, the dilution of Dy(III) ions with Y(III) ions in the excess amount allows the Au(I) centers to emit light in the high energy region (460 nm) and low energy region (around 490 and 510 nm) for the $Dy_{0.1}Y_{0.9}Au$ and $Dy_{0.02}Y_{0.98}Au$. Overall, such changes impact the bluish emission color at 300 K and changes to light blue

ADVANCED
SCIENCE NEWS

www.advancedsciencenews.com

ADVANCED
OPTICAL
MATERIALS

www.advopticalmat.de

and cyan for the $Dy_{0.1}Y_{0.9}Au$ and $Dy_{0.02}Y_{0.98}Au$, respectively, at 100 K (as shown in the inset of Figure 4a–c). The further high-resolution emission spectrum of $Dy_{0.02}Y_{0.98}Au$ helped to understand the splitting of different multiplets for the $^6H_{15/2}$ and $^6H_{13/2}$ (Figure S23, Supporting Information).

The varying luminescence spectra with temperature motivated us to fully characterize the thermometric properties for all three complexes by taking the ratio of emission intensity centered around 575, 480, and 460 nm. The three different thermometric parameters ($\Delta(T)$) are defined by the ratio of emission intensities at 575 to 480 nm, 480 to 460 nm, and 575 to 460 nm (Figure 4d–f). The experimental results reveal different dependencies with temperature for three assemblies. $\Delta(T)$ corresponding to the I_{480}/I_{460} ratio is larger than other thermometric parameters for a wide temperature range. The apparent anomaly can be due to the overlapped luminesce from Dy(III) as well as from the Au(I) centers around this emission region. Since all three luminescence peaks originate from different emissive energy levels, we utilized the Mott–Seitz model given in Equation (4) to fit the experimental data:[19]

$$\Delta(T) = \frac{\Delta_0}{\left[1 + \alpha_1 \exp\left(-\frac{\Delta E_1}{k_B T}\right) + \alpha_2 \exp\left(-\frac{\Delta E_2}{k_B T}\right)\right]} \quad (4)$$

where Δ_0 is the thermometric parameter at $T = 0$ K, α_1, α_2 are the ratio of non-radiative (W_0 at $T = 0$ K) and radiative (W_R) rates, and ΔE_1, ΔE_2 are the activation energies for involved electronic transitions (subscript 1 denotes the nominator, and 2 implies the denominator of the $\Delta(T)$). The fitted parameters are presented in Table S9 (Supporting Information) for all complexes. Fitted results suggest that α_2 and ΔE_2 corresponding to the 460 nm emissive peak are larger than for the 575 and 480 nm within the same thermometric parameter, signifying the differences in photoluminescence origin.

Additionally, the relative thermal sensitivity of the molecular assemblies is evaluated with Equation (5) (Table S10, Supporting Information):

$$S_r = \frac{\left(\frac{\partial \Delta}{\partial T}\right)}{\Delta} \quad (5)$$

The maximum thermal sensitivity for the luminescence thermometer is found in $Dy_{0.02}Y_{0.98}Au$, which is 3.5% K^{-1} at 55 K, 2.4% K^{-1} at 55 K, and 1.8% K^{-1} at 63 K, for the $\Delta(480/460)$, $\Delta(575/460)$, and $\Delta(575/480)$, respectively. Larger sensitivity is associated with the photoluminescence of Au(I) centers varying strongly with temperature due to a closer Au–Au bond at low temperature. For the same reason, thermal sensitivity increases going from DyAu to $Dy_{0.02}Y_{0.98}Au$ through $Dy_{0.1}Y_{0.9}Au$. Temperature uncertainty lies below 1 K for all compounds calculated with the help of $\delta T = (\delta \Delta / \Delta)/S_r$ (Figure S24 and Table S10, Supporting Information). The repeatability of $\Delta(T)$ for all complexes was confirmed by the three cycles of measurement in two different temperature regions (Figures S25–S27, Supporting Information). After considering all the fitted parameters, $Dy_{0.02}Y_{0.98}Au$ is found to be the best temperature sensor among the three complexes; thus, better-performing emission thermometers can be designed by linking structural changes with luminescence.

The comparison of selected materials revealing Raman and/or emission thermometric properties indicates that both temperature sensing methods provide similar sensitivity among high-performing thermometers (**Table 1**) and other fluorescent thermometers (Table S11, Supporting Information). Although some of the luminescence thermometers reveal double-digit sensitivity, they are limited to low-temperature (usually below 10 K) regions. Temperature sensors based on Raman scattering can be characterized sometimes up to

Table 1. Comparison of high-performing thermometer sensitivities for selected Raman and luminescence thermometers at indicated temperatures.

| Raman thermometers				
Materials	Working temperature [K]	Sensitivity	Calculation method	References
$Dy_{0.02}Y_{0.98}Au$	80–300	6.84–0.48% K^{-1}	aS to S peak ratio	This work
DyAu	80–300	6.84–0.48% K^{-1}	aS to S peak ratio	This work
TiO_2	283–323	0.26–0.10% K^{-1}	aS to S peak ratio	[10a]
Silicon wafer	295–433	0.026 cm^{-1} K^{-1}	aS peak position	[20a]
AlGaAs laser diode	300–390	0.026 cm^{-1} K^{-1}	aS peak position	[20a]
Diamond	400–1900	0.033 cm^{-1} K^{-1}	Raman line position (1332 cm^{-1})	[20b]
Luminescence thermometers				
Complexes	Working temperature [K]	Sensitivity	Calculation method	References
$Dy_{0.02}Y_{0.98}Au$	10–300	3.5% K^{-1}@55 K	Two intensities ratio	This work
DyAu	10–300	0.08% K^{-1}@300 K	Two intensities ratio	This work
$[Gd(phen)_2(\mu\text{-}OH)(H_2O)_2] \cdot [Au^I(SCN)_2]_2 \cdot solv$	10–300	6.65% K^{-1}@71 K	Two intensities ratio	[5e]
$NaGdF_4:Pr^{3+}/Er^{3+}@NaYF_4:Yb^{3+}$	83–323	9.5% K^{-1}@83 K	Two intensities ratio	[20c]
Ln–HL (Ln = Eu, Tb)	4–290	31% K^{-1}@4 K	Two intensities ratio	[20d]

aS: anti-Stokes; S: Stokes.

2000 K, providing a very broad working temperature range. In general, Raman thermometers are rarely explored, and other investigated materials include TiO_2, silicon, diamond, etc. Therefore, there is a great need to develop this field with new materials to increase its sensitivity and explore its utility in a wide temperature range.

2.5. Magnetic Properties

Apart from the photophysical properties, the reported materials also exhibit paramagnetic behavior thanks to the Dy(III) ions revealed through direct current (dc) and alternate current (ac) measurements. The magnetic susceptibility-temperature product ($\chi_M T$) versus temperature plot for DyAu indicates that the $\chi_M T$ at 300 K is 13.93 and decreases slowly up to 50 K followed by a sharp drop to 8.25 cm^3 mol^{-1} K at 1.85 K. The observed value for the $\chi_M T$ signal at high temperature is close to theoretically predicted for the $^6H_{15/2}$ ground state of Dy(III) ion. It deviates from the ab initio-calculated curve slightly at low temperatures, which may be due to interatomic interactions (Figure S28, Supporting Information). Magnetization (M) versus field (H) plots at 1.85 K shows the highest value of 5.16 μ_B at 50 kOe which lies in the range typical for paramagnetic Dy(III) ions (Figure S28, Supporting Information). The magnetically diluted samples follow the stochiometric synthetic ratio to resemble the magnetization of pure DyAu. The ac magnetic studies of DyAu reveal SMM behavior; however, at the zero dc field, the out-of-plane χ_M'' signal is out of the measurement range suggesting the dominance of quantum tunneling magnetization (QTM) for spin relaxation (Figure S29, Supporting Information). The proximity of two Dy(III) ions bridged through hydroxide ions may be disadvantageous as it sometimes promotes disturbing antiferromagnetic interaction. Therefore, magnetically diluted samples $Dy_{0.1}Y_{0.9}Au$ and $Dy_{0.02}Y_{0.98}Au$ were examined and the SMM properties under the applied external dc field were detected. (**Figure 5**, Figures S30–S32, and Tables S12–S14, Supporting Information). Relaxation time (τ) versus inverse temperature (T^{-1}) curve for both assemblies is fitted with an Equation describing the Raman, QTM, and Orbach spin relaxation processes (Figure 5, the detailed explanation is given in the Supporting Information). Fitting results suggest that spin–lattice interaction dominates in the magnetization reversal process, which might correlate with the Raman signal observed in the LF region with the vibrational energy of 60 cm^{-1} or lower, suggesting the presence of phonon required to help the spin relaxation to happen through the Raman mechanism.[17] The obtained Orbach energy barrier for $Dy_{0.02}Y_{0.98}Au$ is 90.83 K (63.1 cm^{-1}) following Equation (E3), corroborating the energy gap between the m_J states as predicted through ab initio calculation and underestimating by 63 cm^{-1} calculated with high-resolution emission spectra (Figure S23 and Table S15, Supporting Information). The ground state composition for Dy(III) ions computed by replacing neighboring Dy(III) ions with Y(III) ions reveals that it has an anisotropic magnetic easy axis ($g_z = 18.56$); however accompanied by non-negligible transversal components hampering the zero-dc-field slow magnetic relaxation (Figure S33, Table S15, Supporting Information).

3. Conclusion

We prepared Dy(III)-containing molecular materials with hydroxide bridged bis(lanthanide) moieties crystallizing with dimeric thiocyanido-{Au$^I_2$} units forming emissive excimers. These molecular crystals reveal several sharp peaks in Raman spectra in the LF region related to the various vibrational signatures of the crystal packing. The intensity of the temperature-dependent Raman spectrum decreases with decreasing temperature. The decrease in the Raman scattering is related to the reduction of the phonon mode population following the Boltzmann distribution. Further, to impart temperature sensing abilities to these materials, we selected three peaks of the Raman spectrum located near 27, 108, and 304 cm^{-1} to take the ratio of their anti-Stokes and Stokes Raman shifts. The ratio ρ is fitted to show the good thermometric ability. The maximum sensitivity of 6.84% K^{-1} for vibrational thermometry is observed, corresponding to the highest energy phonon of 304 cm^{-1} as its ρ starts to saturate at the lower temperature region. Additionally, the DyAu crystals are placed inside different benchtop solvents to test their functioning ability as a temperature indicator. For the first time, we presented the ability of these solvents to interfere in the LF region of Raman spectrum measurement. The experiment with acetonitrile resulted in a large background, especially below 50 cm^{-1}. Water, methanol, ethanol, isopropanol, hexane, and acetone did not affect the raw data of the obtained DyAu Raman thermometers. The maximum thermal sensitivity in solvents is observed to be 2.44% K^{-1} relating to the 108 cm^{-1} phonon suggesting the importance of the metal-metal vibrational feature in enhancing the thermometric ability. The vibrational spectroscopy for all the assemblies is also compared with their respective emission thermometric abilities. For these sets of complexes, the observed thermal sensitivity of the luminescence thermometers is lower than the corresponding sensitivity of the Raman thermometer in the entire temperature region. Moreover, observed thermometric ability through Raman and emission spectroscopy for magnetically diluted compound $Dy_{0.02}Y_{0.98}Au$ is better than pure DyAu which also exhibits magnetic relaxation. The improved emission thermometric parameter in $Dy_{0.02}Y_{0.98}Au$ is again related to the emission properties originating from the Au(I) centers, which change exponentially with thermal cooling. Therefore, the dilution of such magnetic matrix improves optical and magnetic properties also observed earlier for Ho(III)-cyanidometallate compounds.[21] In the future, the Raman thermometers' applications, such as the detection of phase-transition of several types of materials, will be explored by mixing the unknown compound with fully characterized Raman thermometers. More extended research should be dedicated to designing high-performing Raman-based temperature sensors functioning in a broad temperature range. This can be done by judiciously selecting the vibrational band with appropriate energy. Moreover, the reported materials reveal SMM behavior that improves upon the magnetic dilution. Spin-lattice relaxation is detected for the magnetically diluted samples, correlating with the vibrational bands of Raman active modes. Therefore, generating or hampering some vibrational features in the LF region should be one of the preconditions for the design of high-performance SMMs, while their presence adds some new functionalities (combination of Raman and luminescent thermometry) as presented here by us.
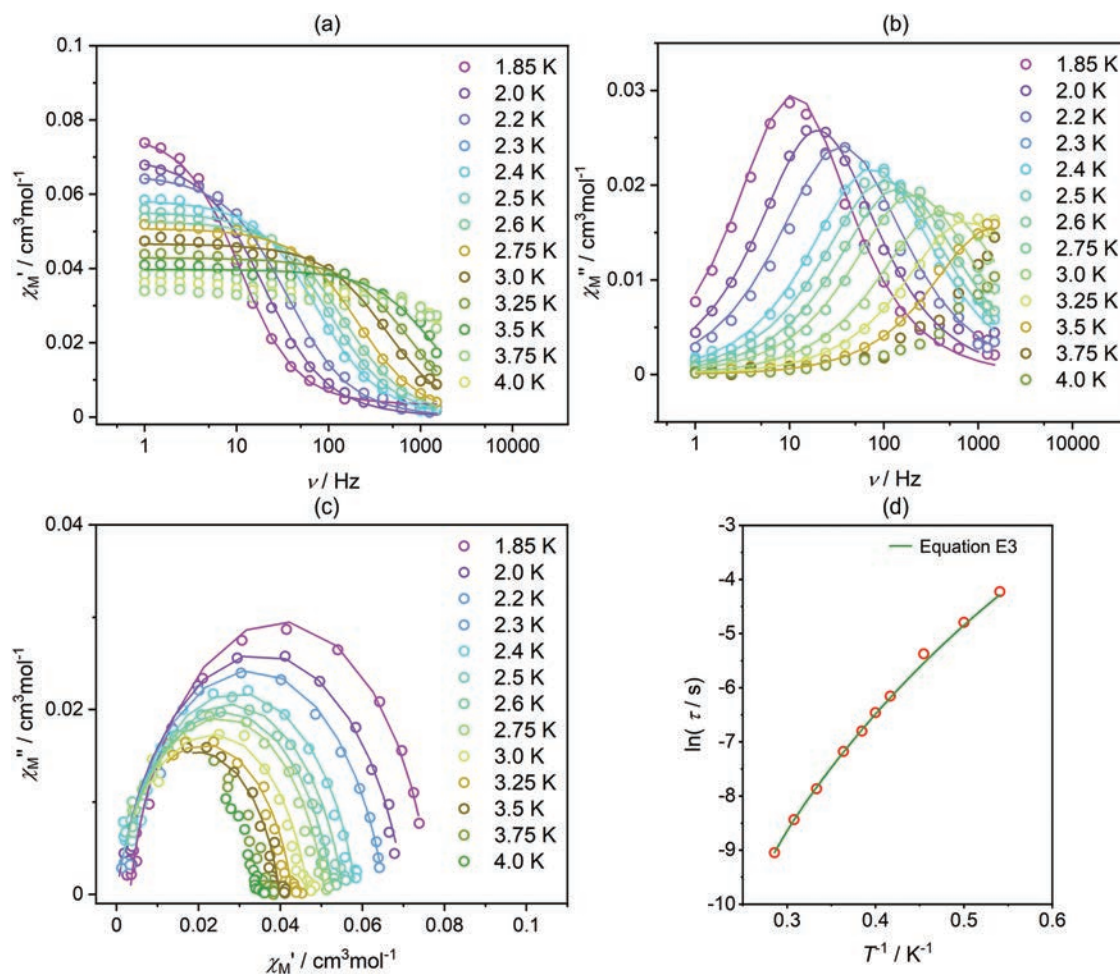
Figure 5. Full *ac* magnetic characteristics of the $Dy_{0.02}Y_{0.98}Au$, under $H_{dc} = 500$ Oe and $H_{ac} = 3$ Oe: frequency (ν) dependences of the in-plane, a) χ_M' and out-of-plane, b) χ_M'' components of the complex magnetic susceptibility for the indicated temperatures of the 1.85–4.00 K range, c) the related χ_M''-χ_M' Argand plots, and d) the temperature dependence of relaxation times (τ) presented as $\ln(\tau)$ versus T^{-1} plot. Solid lines in (a)–(c) were fitted using the generalized Debye model (Table S13, Supporting Information), whereas the solid line in (d) is fitted with Equation (E3) describing QTM, Orbach, and Raman relaxation process (Detailed explanation is provided in Table S14, Supporting Information).

4. Experimental Section

Materials and experimental details are provided in the Supporting Information.

Supporting Information

Supporting Information is available from the Wiley Online Library or from the author.

Acknowledgements

Conflict of Interest

The authors declare no conflict of interest.

Data Availability Statement

The data that support the findings of this study are available from the corresponding author upon reasonable request.

Keywords

[1] a) J.-P. Launay, M. Verdaguer, *Electrons in Molecules: From Basic Principles to Molecular Electronics*, revised ed., Oxford University Press, Oxford, **2017**; b) *Multifunctional Molecular Materials*, Ed. L. Ouahab, Pan Stanford, Singapore, **2013**; c) O. M. Yaghi, M. J. Kalmutzki, C. S. Diercks, *Introduction to Reticular Chemistry: Metal-Organic Frameworks and Covalent Organic Frameworks*, Wiley-VCH, Weinheim, **2019**; d) K. Hashimoto, S. Ohkoshi, *Philos. Trans. R. Soc. London, Ser. A* **1999**, *357*, 2977; e) *Molecular Magnetic Materials: Concepts and Applications*, Eds. B. Sieklucka, D. Pinkowicz, Wiley-VCH, Weinheim, **2017**.

[2] a) O. Kahn, C. J. Martinez, *Science* **1998**, *279*, 44; b) S. Ohkoshi, K. Hashimoto, *J. Photochem. Photobiol., C* **2001**, *2*, 71; c) C. D. S. Brites, A. Millán, L. D. Carlos, *Handbook on the Physics and Chemistry of Rare Earths*, Elsevier, Amsterdam, **2016**, Vol. 49, pp. 339–427; d) Y. Cui, Y. Yue, G. Qian, B. Chen, *Chem. Rev.* **2012**, *112*, 1126; e) X. Meng, H.-N. Wang, S.-Y. Song, H.-J. Zhang, *Chem. Soc. Rev.* **2017**, *46*, 464; f) L. R. Mingabudinova, V. V. Vinogradov, V. A. Milichko, E. Hey-Hawkins, A. V. Vinogradov, *Chem. Soc. Rev.* **2016**, *45*, 5408.

[3] a) C. Train, R. Gheorghe, V. Krstic, L.-M. Chamoreau, N. S. Ovanesyan, G. L. J. A. Rikken, M. Gruselle, M. Verdaguer, *Nat. Mater.* **2008**, *7*, 729; b) C. Train, M. Gruselle, M. Verdaguer, *Chem. Soc. Rev.* **2011**, *40*, 3297; c) R. Sessoli, M.-E. Boulon, A. Caneschi, M. Mannini, L. Poggini, F. Wilhelm, A. Rogalev, *Nat. Phys.* **2015**, *11*, 69; d) S. Ohkoshi, K. Nakagawa, K. Tomono, K. Imoto, Y. Tsunobuchi, H. Tokoro, *J. Am. Chem. Soc.* **2010**, *132*, 6620.

[4] a) T. Nuida, T. Matsuda, H. Tokoro, S. Sakurai, K. Hashimoto, S. Ohkoshi, *J. Am. Chem. Soc.* **2005**, *127*, 11604; b) S. Ohkoshi, K. Nakagawa, K. Imoto, H. Tokoro, Y. Shibata, K. Okamoto, Y. Miyamoto, M. Komine, M. Yoshikiyo, A. Namai, *Nat. Chem.* **2020**, *12*, 338; c) S. Ohkoshi, J. Shimura, K. Ikeda, K. Hashimoto, *J. Opt. Soc. Am.* **2005**, *B 22*, 196; d) S. Ohkoshi, S. Takano, K. Imoto, M. Yoshikiyo, A. Namai, H. Tokoro, *Nat. Photonics* **2014**, *8*, 65.

[5] a) F. Li, X. Wang, Z. Xia, C. Pan, Q. Liu, *Adv. Funct. Mater.* **2017**, *27*, 1700051; b) K. Kumar, S. Chorazy, K. Nakabayashi, H. Sato, B. Sieklucka, S. Ohkoshi, *J. Mater. Chem. C* **2018**, *6*, 8372; c) T. J. Mako, J. M. Racicot, M. Levine, *Chem. Rev.* **2019**, *119*, 322; d) J. Ferrando-Soria, H. Khajavi, P. Serra-Crespo, J. Gascon, F. Kapteijn, M. Julve, F. Lloret, J. Pasan, C. Ruiz-Perez, Y. Journaux, E. Pardo, *Adv. Mater.* **2012**, *24*, 5625; e) K. Kumar, O. Stefanczyk, S. Chorazy, K. Nakabayashi, S. Ohkoshi, *Angew. Chem., Int. Ed.* **2022**, e202201265.

[6] a) J.-X. Wang, T.-S. Zhang, X. Zhu, C.-X. Li, L. Dong, G. Cui, Q.-Z. Yang, *J. Phys. Chem. A* **2020**, *124*, 10082; b) J.-X. Wang, Y.-S. Yu, L.-Y. Niu, B. Zou, K. Wang, Q.-Z. Yang, *Chem. Commun.* **2020**, *56*, 6269; c) S. Liang, Y. Wang, X. Wu, M. Chen, L. Mu, G. She, W. Shi, *Chem. Commun.* **2019**, *55*, 3509; d) M.-J. Sun, Y.-W. Zhong, J. Yao, *Angew. Chem., Int. Ed.* **2018**, *57*, 7820; e) G. Bai, M.-K. Tsang, J. Hao, *Adv. Funct. Mater.* **2016**, *26*, 6330; f) J. Rocha, L. D. Carlos, F. A. Almeida Paza, D. Ananias, *Chem. Soc. Rev.* **2011**, *40*, 926; g) J.-C. G. Bünzli, C. Piguet, *Chem. Soc. Rev.* **2005**, *34*, 1048; h) L. Li, Y. Zhu, X. Zhou, C. D. S. Brites, D. Ananias, Z. Lin, F. A. Almeida Paz, J. Rocha, W. Huang, L. D. Carlos, *Adv. Funct. Mater.* **2016**, *26*, 8677.

[7] a) F. E. Williams, H. Eyring, *J. Chem. Phys.* **1947**, *15*, 289; b) G. F. J. Garlick, A. F. Gibson, *Nature* **1948**, *161*, 359; c) L. Thorington, *J. Opt. Soc. Am.* **1950**, *40*, 579.

[8] X. Chen, Y. Wang, X. Zhang, C. Liu, *Biomater. Sci.* **2021**, *9*, 5484.

[9] a) C. Maher, C. M. Galloway, E. C. Le Ru, L. F. Cohena, P. G. Etchegoin, *Chem. Soc. Rev.* **2008**, *37*, 965; b) E. L. Keller, R. R. Frontiera, *ACS Nano* **2018**, *12*, 5848; c) J. Jaramillo-Fernandez, E. Chavez-Angel, C. M. Sotomayor-Torres, *Appl. Therm. Eng.* **2018**, *130*, 1175; d) S. Sandell, E. Chávez-Ángel, A. El Sachat, J. He, C. M. Sotomayor Torres, J. Maire, *J. Appl. Phys.* **2020**, *128*, 131101.

[10] a) V. Zani, D. Pedron, R. Pilot, R. Signorini, *Biosensors* **2021**, *11*, 102; b) F. Li, H. Wang, R. Huang, W. Chen, H. Zhang, *Adv. Funct. Mater.* **2022**, *32*, 2200516.

[11] D. N. Ngo, V. T. T. X. Ho, G. Kim, M. S. Song, M. R. Kim, J. Choo, S.-W. Joo, S. Y. Lee, *Anal. Chem.* **2022**, *94*, 6463.

[12] C. L. West, A. C. V. Doughty, K. Liu, W. R. Chen, *J. Bio-X Res.* **2019**, *2*, 159.

[13] a) A. Datta, V. Sankar, B. Srinivasan, *ISSS J. Micro. Smart Syst.* **2022**, *11*, 179; b) G. Bolognini, A. Hartog, *Opt. Fiber Technol.* **2013**, *19*, 678.

[14] a) A. De, V. Dwij, V. Sathe, M. A. Hernández-Rodríguez, L. D. Carlos, R. Ranjan, *Physica B* **2022**, *626*, 413455; b) A. De, R. Ranjan, *Mater. Horiz.* **2020**, *7*, 1101.

[15] S. D. McGrane, D. S. Moore, P. M. Goodwin, D. M. Dattelbaum, *Appl. Spectrosc.* **2014**, *68*, 1279.

[16] a) R. Marin, D. Alves Gálico, R. Gayfullina, J. O. Moilanen, L. D. Carlos, D. Jaque, M. Murugesu, *J. Mater. Chem. C* **2022** https://doi.org/10.1039/D2TC01661C; b) K. Karachousos-Spiliotakopoulos, V. Tangoulis, N. Panagiotou, A. Tasiopoulos, E. Moreno-Pineda, W. Wernsdorfer, M. Schulze, A. M. P. Botas, L. D. Carlos, *Dalton Trans.* **2022**, *51*, 8208; c) R. Marin, G. Brunet, M. Murugesu, *Angew. Chem., Int. Ed.* **2021**, *60*, 1728; d) R. A. S. Ferreira, E. Mamontova, A. M. P. Botas, M. Shestakov, J. Vanacken, V. Moshchalkov, Y. Guari, L. F. Chibotaru, D. Luneau, P. S. Andre, J. Larionova, J. Long, L. D. Carlos, *Adv. Opt. Mater.* **2021**, *9*, 2101495; e) K. Kumar, O. Stefanczyk, N. F. Chilton, K. Nakabayashi, K. Imoto, R. E. P. Winpenny, S. Ohkoshi, *Inorg. Chem.* **2021**, *60*, 12009; f) M. Fondo, J. Corredoira-Vazquez, A. M. Garcia-Deibe, J. Sanmartin-Matalobos, M. Amoza, A. M. P. Botas, R. A. S. Ferreira, L. D. Carlos, E. Colacio, *Inorg. Chem. Front.* **2020**, *7*, 3019; g) D. Errulat, R. Marin, D. A. Gálico, K. L. M. Harriman, A. Pialat, B. Gabidullin, F. Iikawa, O. D. D. CoutoJr., J. O. Moilanen, E. Hemmer, F. A. Sigoli, M. A Murugesu, *ACS Cent. Sci.* **2019**, *5*, 1187; h) G. Brunet, R. Marin, M. J. Monk, U. Resch-Genger, D. A. Gálico, F. A. Sigoli, E. A. Suturina, E. Hemmer, M. Murugesu, *Chem. Sci.* **2019**, *10*, 6799; i) K. Kumar, O. Stefanczyk, K. Nakabayashi, K. Imoto, S. Ohkoshi, *CrystEngComm* **2019**, *21*, 5882; j) F. Pointillart, O. Cador, B. Le Guennic, L. Ouahab, *Coord. Chem. Rev.* **2017**, *346*, 150; k) D. N Woodruff, R. E. P. Winpenny, R. A. Layfield, *Chem. Rev.* **2013**, *113*, 5110; l) J. D. Rinehart, J. R. Long, *Chem. Sci.* **2011**, *2*, 2078.

[17] a) J. G. C. Kragskow, J. Marbey, C. D. Buch, J. Nehrkorn, M. Ozerov, S. Piligkos, S. Hill, N. Chilton, *Nat. Commun.* **2022**, *13*, 825; b) D. Reta, J. G. C. Kragskow, N. F. Chilton, *J. Am. Chem. Soc.* **2021**, *143*, 5943; c) K. Kumar, O. Stefanczyk, K. Nakabayashi, Y. Mineo, S. Ohkoshi, *Int. J. Mol. Sci.* **2022**, *23*, 6051.

[18] a) M. Kato, Y. Shichibu, K. Ogura, M. Iwasaki, M. Sugiuchi, K. Konishi, I. Yagi, *J. Phys. Chem. Lett.* **2020**, *11*, 7996; b) K. Bērziņš, S. J. Fraser-Miller, K. C. Gordon, *Int. J. Pharm.* **2021**, *592*, 120034; c) I. Stenger, L. Schué, M. Boukhicha, B. Berini, B. Plaçais, A. Loiseau, J. Barjon, *2D Mater.* **2017**, *4*, 031003.

[19] a) K. Kumar, O. Stefanczyk, K. Nakabayasahi, K. Imoto, Y. Oki, S. Ohkoshi, *Adv. Opt. Mater.* **2022**, *10*, 2101721; b) K. Kumar, K. Abe, K. Komori-Orisaku, O. Stefańczyk, K. Nakabayashi, J. R. Shakirova, S. P. Tunik, S. Ohkoshi, *RSC Adv.* **2019**, *9*, 23444.

[20] a) X. J. Gu, *J. Raman Spectrosc.* **1996**, *27*, 83; b) J. B. Cui, K. Amtmann, J. Ristein, L. Ley, *J. Appl. Phys.* **1998**, *83*, 7929; c) E. M. Rodrigues, D. A. Gálico, M. A. Lemes, J. Bettini, E. T. Neto, I. O. Mazali, M. Murugesu, F. A. Sigoli, *New J. Chem.* **2018**, *42*, 13393; d) X. Liu, S. Akerboom, M. de Jong, I. Mutikainen, S. Tanase, A. Meijerink, E. Bouwman, *Inorg. Chem.* **2015**, *54*, 11323.

[21] J. H. Wang, J. J. Zakrzewski, M. Zychowicz, V. Vieru, L. F. Chibotaru, K. Nakabayashi, S. Chorazy, S. Ohkoshi, *Chem. Sci.* **2021**, *12*, 730.